Epitope Mapping of Antigenic MUC1 Peptides to Breast Cancer Antibody Fragment B27.29: A Heteronuclear NMR Study[†]

Jeffrey S. Grinstead, Jason T. Schuman, and A. Patricia Campbell*

Department of Medicinal Chemistry, School of Pharmacy, University of Washington, Seattle, Washington 98195

Received May 19, 2003

ABSTRACT: MUC1 mucin is a breast cancer-associated transmembrane glycoprotein, of which the extracellular domain is formed by the repeating 20-amino acid sequence GVTSA**PDTRPAP**GSTAPPAH. In neoplastic breast tissue, the highly immunogenic sequence PDTRPAP (in bold above) is exposed. Antibodies raised directly against MUC1-expressing tumors offer unique access to this neoplastic state, as they represent immunologically relevant "reverse templates" of the tumor-associated mucin. In a previous study [Grinstead, J. S., *et al.* (2002) *Biochemistry 41*, 9946−9961], ^{1}H NMR methods were used to correlate the effects of cryptic glycosylation outside of the PDTRPAP core epitope sequence on the recognition and binding of Mab B27.29, a monoclonal antibody raised against breast tumor cells. In the study presented here, isotope-edited NMR methods, including ^{15}N and ^{13}C relaxation measurements, were used to probe the recognition and binding of the PDTRPAP epitope sequence to Fab B27.29. Two peptides were studied: a one-repeat MUC1 16mer peptide of the sequence GVTSAPDTRPAPGSTA and a two-repeat MUC1 40mer peptide of the sequence (VTSAPDTRPAPGSTAPPAHG)$_2$. ^{15}N and ^{13}C NMR relaxation parameters were measured for both peptides free in solution and bound to Fab B27.29. The ^{13}C$_\alpha$ T_1 values best represent changes in the local correlation time of the peptide epitope upon binding antibody, and demonstrate that the PDTRPAP sequence is immobilized in the antibody-combining site. This result is also reflected in the appearance of the ^{15}N- and ^{13}C-edited HSQC spectra, where line broadening of the same peptide epitope resonances is observed. The PDTRPAP peptide epitope expands upon the peptide epitope identified previously in our group as PDTRP by homonuclear NMR experiments [Grinstead, J. S., *et al.* (2002) *Biochemistry 41*, 9946−9961], and illustrates the usefulness of the heteronuclear NMR experiments. The implications of these results are discussed within the context of MUC1 breast cancer vaccine design.

Mucins have been implicated as targets for vaccine development in cancers of the breast, colon, pancreas, lung, and ovary because of the differences between normal and tumor-associated mucin (*1−4*). Mucin 1 (MUC1)[1] is a large transmembrane glycoprotein that is expressed on the ductal surface of epithelial cells. The extracellular region of the protein consists of a variable number of tandem repeats (VNTR) of the 20-amino acid sequence (GVTSA**PDTR-P**APGSTAPPAH)$_n$, extensively O-glycosylated at threonine and serine sites with large, branched sugars (*5−8*). However, in the tumor-associated state, MUC1 becomes an autoantigen as a result of incomplete glycosylation and the sparse distribution of remaining carbohydrate structures (*9*). The reduced level of glycosylation is believed to result in the exposure of a highly immunogenic core peptide sequence (PDTRP in bold above) (*10*), identified as the immunodominant B-cell epitope from monoclonal antibody studies in mice (*11−15*). This PDTRP core peptide sequence is also believed to be immunodominant in humans. Breast cancer patients with MUC1-expressing tumors develop limited humoral and cellular immune responses against the tumor (*16−18*), with the elicited antibodies and T-cells cross-reactive to the PDTRP core peptide sequence (*19−21*).

Many different clinical trials have been undertaken over the past few years to assess the ability of MUC1-based vaccines to generate strong and cytotoxic anti-MUC1 immune responses against the solid MUC1-expressing tumor. Several of these trials have explored the use of MUC1 peptides coupled to different haptens, keyhole limpet hemocyanin, oxidized mannan, and glutathione *S*-transferase (*4*). In addition, at least two different vaccine trials have used MUC1-associated antigenic sugars (without peptide) (*22*). Other more recent clinical trials have utilized peptide- or DNA-pulsed dendritic cells as vaccine vectors, attempting to capitalize on the superior immune activation by these antigen-presenting cells. Dendritic cells pulsed with either MUC1 peptides or cDNA have been able to generate limited CD8$^+$ T-cell responses to solid breast tumors (*23*, *24*), although these responses did not result in tumor rejection.

* To whom correspondence should be addressed: Department of Medicinal Chemistry, School of Pharmacy, University of Washington, Seattle, WA 98195. Telephone: (206) 685-2468. Fax: (206) 685-3252. E-mail: apc@u.washington.edu.

[1] Abbreviations: DSS, 2,2-dimethyl-2-sila-5-pentanesulfonate; Fab, antigen-binding fragment of monoclonal antibody; Mab, monoclonal antibody; MUC1, mucin-1; NMR, nuclear magnetic resonance; NOE, nuclear Overhauser effect; NOESY, 2D nuclear Overhauser effect spectroscopy; HSQC, heteronuclear single quantum coherence.

Indeed, none of the MUC1 vaccine candidates described above have been shown to be effective at tumor rejection, although the reasons for this are not absolutely clear (25−29).

The failure of MUC1-based vaccines to generate effective immune responses may stem from the use of vaccine candidates that do not represent the structure, dynamics, peptide epitope exposure, or even glycosylation state of the tumor-associated mucin. For example, vaccination with a MUC1 peptide is unlikely to generate an immune response to the heavily glycosylated region of the extracellular domain of MUC1 on the surface of healthy epithelial cells. While this situation should limit the possibility of an autoimmune response against healthy epithelial tissues, it is also unlikely to lead to a strong tumor-specific immune response against the partially glycosylated tumor-associated MUC1 protein.

In an effort to better characterize the glycosylation state and peptide epitope exposure of the tumor-associated MUC1 protein, many *in vitro* and *in vivo* glycosylation studies have been undertaken. *In vitro* glycosylation studies using human tumor cell extracts (30−32) have demonstrated the presence of cryptic carbohydrate structures at only three sites in the sequence (GVTSA and GSTAP), and not at the central threonine within the PDTRP core peptide epitope region. However, recent *in vivo* studies have demonstrated that all five sites are glycosylation targets in the tumor cell (33, 34). Thus, the glycosylation state of the tumor-associated MUC1 mucin remains indeterminate at present. Furthermore, while spectroscopic techniques such as NMR and CD have identified native β-turn secondary structure in unglycosylated MUC1 (35−40), these studies have not been extrapolated to the intact partially glycosylated MUC1 protein as it exists *in situ* on the tumor cell surface. In the absence of a clear and definitive picture of the MUC1 mucin in its tumor-associated state, the design of a peptide or glycopeptide vaccine that mimics this "unknown" state is a difficult undertaking.

To circumnavigate this difficulty, we propose an approach that does not rely on *a priori* knowledge of the peptide conformation or glycosylation state for the tumor-associated MUC1 mucin. This alternative approach involves the use of an anti-MUC1 antibody, Mab B27.29, as a "reverse template" for MUC1 vaccine design. Mab B27.29 was raised directly against MUC1-expressing tumors, so should bind most tightly to a MUC1 peptide or glycopeptide that best approximates the structure, dynamics, and glycosylation state of the tumor-associated mucin. As such, Mab B27.29 is an immunologically relevant reverse template of the structure, dynamics, and chemistry of the tumor-associated MUC1 mucin. In brief, this approach identifies the immunologically relevant peptide conformation and glycosylation states of the tumor-associated MUC1 mucin by probing the structure and dynamics of MUC1 peptide−Mab B27.29 recognition and binding. Solution-state NMR is used as the probe in these systems, as it allows both structure and dynamics information to be obtained for the bound state, even if that bound state is dynamic and conformationally heterogeneous.

Using this NMR-based approach, we recently completed a homonuclear NMR study examining the effect of glycosylation on Fab B27.29 recognition of a series of 16-residue MUC1 glycopeptides of the sequence GVTSAPDTRPAPG-STA (37). The results of this study showed that the B27.29 epitope maps to two separate parts of the glycopeptide, the core peptide epitope spanning the PDTRP sequence and a second (carbohydrate) epitope comprised of two cryptic carbohydrate moieties attached at Thr3 and Ser4 in the 16mer sequence. The results of this study also showed that the peptide and carbohydrate epitopes bind independently of each other to Fab B27.29, prompting us to further explore the contributions of each epitope separately. In the study presented here, we extend our NMR-based approach to include heteronuclear NMR studies of the role of peptide structure and dynamics on Fab B27.29 recognition of the same 16-residue MUC1 peptide, as well as of a 40-residue MUC1 peptide [(VTSAPDTRPAPGSTAPPAHG)$_2$] that represents two repeats of the MUC1 sequence. Future studies will continue this line of research in an effort to analyze the role of carbohydrate structure and dynamics in glycopeptide−antibody recognition.

NMR studies probing the structure and dynamics of the 16- and 40-residue MUC1 peptides in free versus Fab-bound states are significantly facilitated by our ability to generate isotopically labeled recombinant peptides. This allows for the acquisition of isotope-edited NMR experiments of the MUC1 peptide−B27.29 antibody complex, offering a significant increase in the amount of information relative to our previous efforts with simple homonuclear NMR experiments. Included in this study are two-dimensional isotope-edited NMR experiments, as well as heteronuclear NMR relaxation measurements, monitoring the binding of the isotopically labeled MUC1 peptides to the unlabeled Fab fragment of B27.29. These experiments allow a precise mapping of the boundary of the B27.29 epitope, based on a determination of the immobilized portion of the peptide as it is bound within the B27.29 antibody-combining site. The results of these studies are discussed within the framework of developing a second-generation MUC1 peptide vaccine that better represents the peptide portion of the tumor-associated MUC1 mucin, as it is recognized *in situ* by B27.29.

MATERIALS AND METHODS

Peptide and Fab Samples. Fab (∼50 kDa) was generated by papain and pepsin cleavage of IgG B27.29, and was a generous gift from Biomira Inc. (Edmonton, AB).

Cloning of 16mer and 40mer Peptides. Two MUC1 sequences derived from the extracellular domain of the MUC1 protein were cloned and expressed for the purposes of this study: (1) a one-repeat 16mer MUC1 sequence (Gly1-Val2-Thr3-Ser4-Ala5-Pro6-Asp7-Thr8-Arg9-Pro10-Ala11-Pro12-Gly13-Ser14-Thr15-Ala16) and (2) a two-repeat 40mer MUC1 sequence (Val1-Thr2-Ser3-Ala4-Pro5-Asp6-Thr7-Arg8-Pro9-Ala10-Pro11-Gly12-Ser13-Thr14-Ala15-Pro16-Pro17-Ala18-His19-Gly20-Val21-Thr22-Ser23-Ala24-Pro25-Asp26-Thr27-Arg28-Pro29-Ala30-Pro31-Gly32-Ser33-Thr34-Ala35-Pro36-Pro37-Ala38-His39-Gly40). These two 16mer and 40mer MUC1 sequences were expressed as ^{15}N- and ^{13}C-labeled recombinant peptides in *Escherichia coli* using a methodology described previously (41). Briefly, genes with multiple repeats of MUC1 DNA sequences were constructed from purchased oligonucleotides, purified, and ligated into plasmid DNA vector pET-31b(+). The MUC1 16mer and 40mer DNA-containing plasmids were separately trans-

formed into the competent *E. coli* BLR(DE3) strain for protein expression. Isotopically ^{15}N- and ^{13}C-labeled peptides were then expressed by growing the transformed bacteria in minimal medium containing M9 salts, and with ^{15}NH$_4$Cl and [^{13}C$_6$]glucose as the sole sources of nitrogen and carbon, respectively. Isotopically labeled minimal medium was inoculated at an OD$_{600}$ of 0.1 from an overnight culture, and grown to an OD$_{600}$ of 0.6−0.8 before induction of protein expression with 1 mM IPTG. Induced cultures were grown overnight before cells were harvested by centrifugation.

Harvested cell pellets were lysed by sonication, and the insoluble fraction was collected by centrifugation. The insoluble fraction was washed several times with Tris buffer (50 mM, pH 8), and then solubilized using 4 M guanidine hydrochloride-containing Tris buffer. The solubilized fusion protein was purified using nickel column chromatography under denaturing conditions of 4 M guanidine. The purified fusion protein was eluted from the column with a linear gradient of 4 to 500 mM imidazole. Fractions containing protein were dialyzed against water overnight, exchanging with freshwater several times. The water-insoluble fusion protein precipitate was collected by centrifugation.

The expressed fusion protein was designed with methionine residues separating the insoluble KSI domain from the inserted MUC1 peptide sequence, between each repeat of the MUC1 peptide sequence, and before the histidine tag. The fusion was digested with an excess of CNBr in 88% formic acid under nitrogen gas overnight at room temperature to cleave at all methionine residues and leave a homoserine lactone at the C-terminus of all fragments. Formic acid was removed by rotary evaporation, and the products were stirred in distilled water. The insoluble KSI domain remained as a precipitate, and was removed by centrifugation. The soluble peptide cleavage products were lyophilized and resuspended in a 90% H$_2$O/10% acetonitrile mixture for HPLC purification.

MUC1 peptides were purified using reverse-phase HPLC on a prep scale radial compression C18 column (Alltech). MUC1 peptides were eluted with a linear gradient of 10 to 95% acetonitrile. One major peak was observed in most cases, which eluted with the same retention time as a standard synthetic MUC1 peptide. Fractions containing purified MUC1 peptides were collected, and the volatile solvents were removed by rotary evaporation. The remaining aqueous solutions lyophilized to give the pure peptide with a yield of 17 mg of isotope-labeled peptide per liter of minimal medium (50 mg/L for unlabeled peptide in LB medium).

Fluorescence Binding Measurements. Fluorescence measurements were used to determine the equilibrium dissociation constants (K_D) and kinetic off rates (k_{-1}) for the binding of the MUC1 16mer and 40mer peptides to Fab B27.29. Fab B27.29 (0.86 μM stock solution) was titrated with small aliquots of peptide to a final concentration that was more than 200-fold in excess of the Fab concentration. The change in Fab fluorescence intensity was monitored, and the concentration of bound ligand was calculated (percent of maximum fluorescence change). The natural log of the free ligand concentration was plotted against the concentration of the bound ligand, and the curve was fit to eq 1

$$[\text{bound}] = (\text{capacity}[\text{free ligand}])/(K_D + [\text{free ligand}]) \tag{1}$$

according to Michaelis−Menten kinetics, where the capacity is the concentration of the Fab and K_D is the equilibrium dissociation constant.

Titration of Fab with Peptides. Samples for NMR spectroscopy were dissolved in 90% H$_2$O, 10% D$_2$O PBS, 1 mM DSS, and 0.01% NaN$_3$ and adjusted to pH 7.1 (uncorrected for D$_2$O concentration). Titrations were performed on samples containing 200 μM Fab B27.29 (by mass), with the MUC1 16mer peptide at 40, 80, 140, 200, 500, 800, and 1600 μM and the 40mer peptide at 80, 160, 240, 320, 400, 800, and 1200 μM. Peptide was added from concentrated 30 mM stock solutions to minimize dilution of the Fab sample. At the final titration point, dilution of the Fab sample was less than 5%. The concentrations of the stock peptide solutions were determined by comparing the one-dimensional (1D) NMR integration of peptide peaks relative to an external DSS standard that was calibrated against the primary standard potassium hydrogen phthalate. At each titration point, ^{1}H NMR spectra were obtained, as well as ^{1}H−^{15}N HSQC and ^{1}H−^{13}C HSQC spectra. At select titration points, ^{15}N T_1, ^{15}N T_2, {^{1}H}−^{15}N NOE, ^{13}C$_\alpha$ T_1, and ^{13}C$_\alpha$ $T_{1\rho}$ measurements were also taken. The {^{1}H$_\alpha$}−^{13}C$_\alpha$ NOE data sets were obtained by lyophilizing the samples and resuspending them in 99.9% D$_2$O to aid in water suppression.

NMR Experiments. Most NMR experiments were performed on a Varian Inova 500 MHz spectrometer at 5 °C. Triple-resonance and ^{15}N-edited NOESY-HSQC experiments to identify Fab-bound peptide resonances were carried out on a Varian Inova 750 MHz spectrometer at 5 °C. All NMR spectra were referenced to DSS at 0 ppm. Proton NMR resonances were assigned as previously reported (*37*). Carbon and nitrogen resonances were assigned using the known proton chemical shifts in the ^{1}H−^{15}N HSQC and ^{1}H−^{13}C HSQC spectra, as well as a three-dimensional (3D) ^{1}H−^{15}N NOESY-HSQC experiment. 1D ^{1}H NMR spectra were acquired at 5 °C, with a spectral width of 7000 Hz, using 32 000 acquired points. ^{1}H−^{15}N HSQC spectra were typically acquired using a spectral width of 1114 Hz and 32 points in t_1 and a spectral width of 7000 Hz and 2048 points in t_2. ^{1}H−^{13}C HSQC spectra of α-carbon−proton pairs were typically acquired using a spectral width of 3000 Hz and 48 points in t_1 and a spectral width of 7000 Hz and 2048 points in t_2. Relaxation experiments utilized similar parameters. ^{15}N T_1 experiments recorded spectra with relaxation delays of 10.3, 51.3, 102.5, 153.8, 205, 307.5, and 410 ms, with duplicate experiments recorded for the 51.3 ms data point to confirm our error estimates. ^{13}C$_\alpha$ T_1 experiments recorded spectra with relaxation delays of 10, 50, 100, 150, 200, and 300 ms, with the 100 ms data set duplicated for confirmation of error estimates. ^{15}N T_2 experiments recorded spectra with relaxation delays of 14.4, 28.8, 57.6, 86.4, 115.2, 144, and 158.4 ms, with a duplicate data set at 57.6 ms. ^{13}C$_\alpha$ $T_{1\rho}$ experiments recorded spectra with relaxation delays of 10, 20, 40, 60, 100, 150, 200, and 250 ms, with the 40 ms data set duplicated for confirmation of error estimates. Steady-state {^{1}H}−^{15}N NOE and {^{1}H$_\alpha$}−^{13}C$_\alpha$ NOE experiments were performed with and without a 3 s presaturation period. During this presaturation period,

proton frequencies were irradiated with a continuous low-power pulse. In the experiment without presaturation, the low-power irradiation was replaced with a delay period of 3 s. The NOE values were calculated as the ratio of peak intensities in the experiments with and without proton presaturation. Pulse sequences were utilized as reported previously (*42*, *43*).

Triple-resonance HNCACB (*44*) and CBCA(CO)NNH (*45*) experiments were performed at 750 MHz to assign the bound peptide resonances that appeared in the Fab-bound spectra. The MUC1 16mer peptide was used for these experiments because of its spectral simplicity. The MUC1 16mer (250 μM) was added to Fab B27.29 (200 μM) to achieve the highest intensity for the Fab-bound resonances without complicating the spectra with resonances from the free MUC1 16mer. Two-dimensional (2D) versions of the HNCACB and CBCA(CO)NNH experiments were employed, because under the sample conditions that were used, and with the greater spectral dispersion of the higher magnetic field strength of 750 MHz, the amide protons of interest were resolved from all other resonances. The HNCACB experiment was carried out using 1000 transients and 1024 complex points in the acquired dimension, 120 complex points in the indirect carbon dimension, and sweep widths (750 MHz) of 15 100 Hz for carbons and 10 500 Hz for protons. The CBCA(CO)NNH experiment was carried out using 2048 transients and 1024 complex points in the acquired dimension, 80 complex points in the indirect carbon dimension, and sweep widths (750 MHz) of 11 000 Hz for carbons and 10 500 Hz for protons. In addition, a 2D ^{15}N-edited NOESY-HSQC experiment was carried out at 750 MHz on the same MUC1 16mer–Fab B27.29 sample. This experiment utilized 1216 transients and 1024 complex points in the acquired dimension, 188 points in the indirect proton dimension, and sweep widths (750 MHz) of 7500 Hz for the indirect proton and 10 500 Hz for the acquired proton dimensions.

Data Processing and Analysis. All 2D data sets were processed on a Silicon Graphics O2 workstation using the NMRPipe System software (*46*). In both dimensions, 2D data sets were multiplied by a 90°-shifted squared sine bell and zero-filled prior to Fourier transformation. T_1 and T_2 values were determined using nonlinear least-squares fitting of the measured peak heights to a two-parameter exponential decay, also within the NMRPipe package. Uncertainties in the calculated T_1 and T_2 values from the least-squares fitting were determined by the signal-to-noise ratio of individual peaks in each of the T_1 and T_2 experiments (*42*, *43*). Two groups have recently shown error estimates from least-squares fitting to be unreasonably small, and have used the value of 5% as a more realistic value (*47*, *48*). Therefore, we have set the error in the calculated T_1 and T_2 to 5% of the values.

Reduced Spectral Density Mapping. Reduced spectral density mapping is a convenient method for characterizing the motion of each N–H bond at $J(0)$, $J(\omega_N)$, and $J(\omega_H)$ frequencies (*49*, *50*). The spectral densities at these three frequencies can be obtained from relaxation rates R_1 ($1/T_1$) and R_2 ($1/T_2$) and the steady-state heteronuclear NOE using eqs 2–4.

$$J(\omega_H) = [4/(5d^2)](\gamma_N/\gamma_H)(\text{NOE} - 1)/T_1 \quad (2)$$

$$J(\omega_N) = [1/T_1 - (7d^2/4)J(\omega_H)]/(3d^2/4 + c^2) \quad (3)$$

$$J(0) = [1/T_2 - (3d^2/8 + c^2/2)J(\omega_N) - \\ (13d^2/8)J(\omega_H)]/(d^2/2 + 2c^2/3) \quad (4)$$

For the above equations, $d = [\mu_0 h(\gamma_N\gamma_H)/8\pi^2]\langle 1/r_{NH}^3\rangle$ and $c = (\omega_N/3^{1/2})(\sigma_\parallel - \sigma_\perp)$, and ω_N and ω_H are the Larmor frequencies of the ^{15}N and ^{1}H nuclei, respectively.

RESULTS

Assignment of Resonances. ^{1}H, ^{15}N, and ^{13}C resonance assignments for the ^{15}N- and ^{13}C-labeled recombinant MUC1 16mer and 40mer peptides are shown in Table S1 of the Supporting Information.

Fluorescence Binding Measurements. The equilibrium dissociation constant (K_D) for a ligand binding to a macromolecule is equal to the ratio of the intrinsic kinetic on (k_1) and off (k_{-1}) rate constants.

$$K_D = \frac{k_{-1}}{k_1} \quad (5)$$

Fluorescence binding measurements were used to determine the K_D, k_{-1}, and stoichiometry for the binding of the MUC1 16mer and 40mer peptides to Fab B27.29. These experiments yielded a K_D of 10.9 ± 0.4 μM for the 16mer and a K_D of 11.1 ± 0.5 μM for the 40mer, with 1:1 binding stoichiometry measured in each case.

Exchange Time Scales of MUC1 Peptide–Fab B27.29 Binding. Using the K_D values measured from the fluorescence binding titrations, we have attempted to establish off-rates and time scales for the binding of the MUC1 16mer and 40mer peptides to Fab B27.29, a prerequisite for accurate NMR data interpretation. Surface plasmon resonance experiments in other systems indicate that a diffusion-controlled on rate (10^8 M^{-1} s^{-1}) is not a valid assumption for a flexible peptide binding to solution-state Fab. On the basis of estimates for similar complexes (*51*–*54*), we therefore assume a value of 10^6–10^7 M^{-1} s^{-1} for the kinetic association rate k_1. Combining this value with the measured equilibrium binding constant K_D (eq 5) gives a kinetic dissociation rate k_{-1} of 10–100 s^{-1}.

The first relevant NMR time scale to be considered is the chemical shift time scale. Intermediate exchange on the chemical shift time scale ($k_{-1} \sim \Delta\delta$)[2] is expected for the majority of peptide resonances in the MUC1–B27.29 complex, as a k_{-1} of 10–100 s^{-1} is within the range of the typical differences between free and bound chemical shifts [$\Delta\delta = 100$–1000 Hz (*55*)]. In this regime, MUC1 peptide resonances are not expected to shift with varying concentration of ligand, but instead experience a loss in signal intensity due to line broadening (*55*). However, the MUC1–B27.29 system is additionally complicated due to portions of the peptide coexisting on different exchange time scales, contingent on the relative magnitudes of the $\Delta\delta$ terms (which vary across the peptide sequence). For example, peptide

---

[2] $\Delta\delta$ represents the difference between the frequencies of the exchanging free and bound peptide resonances ($\Delta\delta = |\delta B - \delta F|$).

resonances belonging to the Fab binding epitope residues PDTRPAP, which are expected to have the largest $\Delta\delta$ terms, may experience slow exchange on the chemical shift time scale ($k_{-1} \ll \Delta\delta$). In this regime, distinct free and bound MUC1 peptide resonances would be expected at their respective chemical shifts. Conversely, smaller $\Delta\delta$ values for resonances at the MUC1 peptide termini could well translate into fast exchange on the chemical shift time scale ($k_{-1} \gg \Delta\delta$). This third regime, if present, would be characterized by a single MUC1 peptide resonance at the population-weighted average of the free and bound chemical shifts. Thus, we anticipate a mixture of exchange regimes for MUC1 peptide resonances in an HSQC-monitored Fab B27.29 titration, marked by complex spectral behavior.

Another relevant NMR time scale to be considered is the relaxation time scale. Relaxation parameters such as the spin−lattice relaxation rate (R_1), spin−spin relaxation rate (R_2), and steady-state heteronuclear NOE are characterized by rate differences between their free and bound states that are smaller than those associated with chemical shift. For example, typical differences cited in the literature are 0.1−10 Hz for R_1, 1−50 Hz for R_2, and 0.1−5 Hz for NOE (*55*). Thanks to these faster time scales, a k_{-1} of $10-100$ s^{-1} puts the MUC1 peptide−Fab system in the fast exchange limit with respect to spin relaxation ($k_{-1} \gg R_{1B}$, where $R_{1B} = 1/T_{1B}$, the spin−lattice relaxation rate of the bound state). In this regime, relaxation properties of the bound state are transferred to the resonances of the free state, and the observed R_1 is a population-weighted average of the free and bound R_1 values [eq 6 (*56*)].

$$R_{1obs} = P_B R_{1B} + P_F R_{1F} \qquad (6)$$

The same principle allows implementation of the TRNOESY experiment (*57*). We have previously shown that the MUC1 peptide experiences a significant transferred NOESY effect upon binding to Fab B27.29 (*37*), providing further credence that the system is in fast exchange with respect to the NMR relaxation time scale.

The existence of two exchange regimes for the MUC1 system, intermediate on the chemical shift time scale, but fast on the relaxation time scale, allows dynamics information to be obtained for the bound state, regardless of whether an averaged resonance is monitored (fast exchange on the chemical shift time scale), an exchange-broadened resonance is monitored (intermediate exchange on the chemical shift time scale), or separate free and bound resonances are monitored (slow exchange on the chemical shift time scale). An interesting corollary of this condition is that these separate free and bound MUC1 resonances should also manifest the same line width, as line widths are largely dependent on spin−spin relaxation rates, and these rates are population-weighted averages in the limits of fast exchange with respect to relaxation.

15N HSQC-Monitored Titrations of MUC1 Peptides with Fab B27.29. Panels A and C of Figure 1 present the ^{15}N-edited HSQC spectra acquired for the ^{15}N- and ^{13}C-labeled 16mer and 40mer MUC1 peptides, respectively, in the absence of Fab B27.29. A cursory examination of these spectra reveals that the chemical shifts for residues APDTR-PAPGSTA are almost identical for the two peptides (i.e., the peaks representing A5−A16 in the 16mer sequence are

roughly superimposable with the peaks representing A4−A15 in the 40mer sequence). This suggests that the PDTR-PAP epitope regions in the 16mer and 40mer explore similar, if not identical, conformational space. Further examination of just the 40mer HSQC spectrum (Figure 1C) reveals that the peaks corresponding to residues PDTRPAPGSTA (D6/16−A18/38) are chemical shift degenerate, indicating that the conformational space explored by the core peptide epitope is identical from one repeat to the next. A full characterization of the dependence of MUC1 structure and dynamics on the number of repeat sequences is presented elsewhere (*58*). However, previous ^{1}H NMR studies published by this group have identified a well-populated type I β-turn spanning residues PDTR within the PDTRPAP epitope region (*37, 38, 58*). As the β-turn is a common structural motif in antigenic regions of proteins (*59*), and is commonly found in NMR and crystal structures of antibody−antigen complexes (*60−63*), the presence of a β-turn within the MUC1 B-cell epitope may explain the immunodominance of this region.

Panels B and D of Figure 1 present the ^{15}N-edited HSQC spectra acquired for the ^{15}N- and ^{13}C-labeled 16mer and 40mer MUC1 peptides, respectively, in the presence of Fab B27.29. These spectra correspond to the first titration point with a molar ratio of peptide to Fab of greater than unity ([peptide]/[Fab] > 1), a point at which resonances for the significantly exchange broadened residues within the PDTR-PAP epitope region could begin to be detected. These resonances correspond to D7, T8, R9, A11, and G13 within the 16mer (boxed in Figure 1B) and D6/26, T7/27, R8/28, A10/30, and G12/32 within the 40mer (boxed in Figure 1D), an identical collection of residues that indicates an identical mode of epitope recognition and binding in the one-repeat and two-repeat systems.

As predicted, complex spectral behavior is observed in panels B and D of Figure 1, marked by a mixture of chemical shift exchange time scales. For example, extensive line broadening consistent with an intermediate exchange time scale ($k_{-1} \sim \Delta\delta$) renders the PDTRPAP resonances unobservable until the Fab is saturated ([peptide]/[Fab] > 1) and a significant pool of free peptide is allowed to build up. In contrast, MUC1 residues outside the PDTRPAP epitope sequence display sizable peaks, even when [peptide]/[Fab] < 1(see Figure 2A,B), at which point all of the peptide would be expected to be in the Fab-bound pool. The intensities of these peaks increase with an increasing concentration of peptide, and resonate at or near their free chemical shifts ($\Delta\delta \sim 0$), implying no change in the chemical environment upon Fab binding and therefore little or no contact with the antibody-combining site. This behavior is consistent with fast exchange on the chemical shift time scale ($k_{-1} \gg \Delta\delta$), as predicted for residues at the MUC1 peptide termini.

Finally, Figure 1B shows one of several new peaks in the Fab-bound spectrum of the 16mer (marked with an asterisk in the spectrum). These peaks appear at the lowest concentrations of MUC1 peptide, and increase in intensity with peptide concentration until the Fab is saturated with peptide, and the free peptide peaks of the bound epitope sequence begin to appear in the spectrum (see Figure 2). In other words, these new bound peptide peaks display classic slow exchange titration behavior. Similar bound resonances are
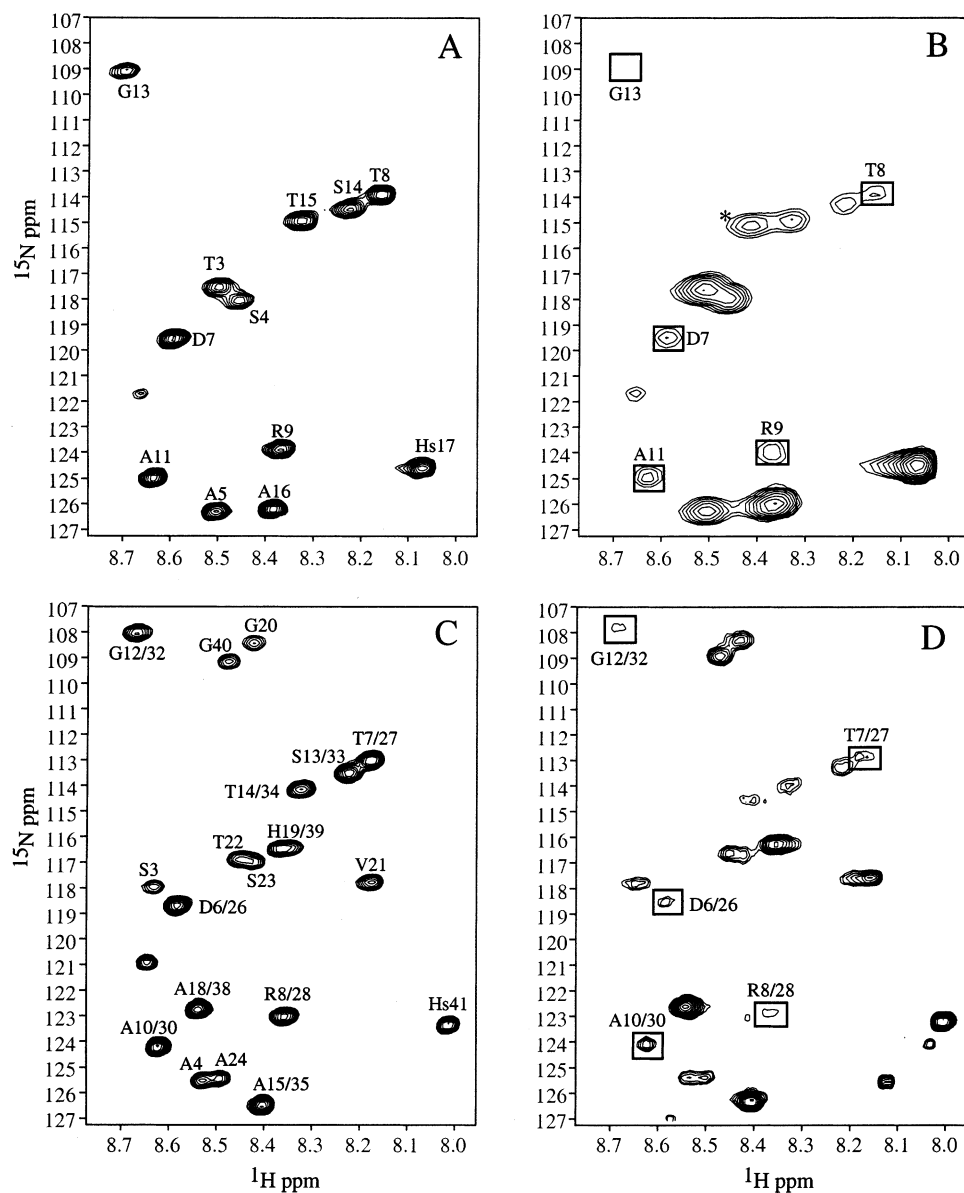
FIGURE 1: $^1H-^{15}N$ HSQC spectra of (A) 800 μM MUC1 16mer free in solution, (B) 500 μM 16mer with 200 μM Fab B27.29, (C) 800 μM 40mer free in solution, and (D) 320 μM 40mer with 200 μM Fab B27.29. Boxed cross-peaks experience the greatest losses in signal intensity due to line broadening in the presence of Fab. The spectra for the peptide with or without Fab were recorded at 500 MHz on a Varian Inova 500 NMR spectrometer. NMR samples were in PBS buffer (pH 7.1) and 90% H_2O/10% D_2O at 5.0 °C.

also seen in the $^1H-^{15}N$ HSQC spectrum of the 40mer. As these new 16mer peaks are absent in the free peptide spectrum, they must correspond to a set of bound peptide resonances that experiences slow exchange on the chemical shift time scale ($k_{-1} \ll \Delta\delta$). Interestingly, only two new bound peptide resonances are observed with strong intensity, not four bound peptide resonances as might be expected since the PDTRPAP epitope sequence contains four non-proline residues. Therefore, these two bound peptide resonances must represent a subset of residues within the peptide epitope that experience the greatest change in chemical environment upon Fab binding (the largest $\Delta\delta$ terms), and thus the most intimate contact with the antibody-combining site. To probe further the identities of these bound peptide resonances, triple-resonance experiments were performed. Although chemical exchange broadening of most epitope resonances within the PDTRPAP sequence prohibits complete assignment of the observed bound-state resonances, the triple-resonance experiments confirm that the new peak at 8.51

ppm in the $^1H-^{15}N$ HSQC spectrum of the 16mer (marked with an asterisk in Figures 1B and 2) is from R9. This conclusion is supported by mutational analysis demonstrating that the presence of R9 in the MUC1 sequence is necessary for binding to other breast and ovarian cancer antibodies (*12*).

^{13}C HSQC-Monitored Titrations of MUC1 Peptides with Fab B27.29. The ^{13}C-edited HSQC spectra acquired for the ^{15}N- and ^{13}C-labeled 16mer and 40mer MUC1 peptides in the absence (Figure 3A,C) and presence (Figure 3B,D) of Fab B27.29 are also shown. These ^{13}C-edited HSQC spectra provide chemical shift information for the many proline residues in the MUC1 sequences, as well as for select side chain resonances. As previously noted for Figure 1, AP-DTRPAPGSTA backbone and side chain resonances are chemical shift degenerate in the 16mer versus the 40mer spectra, and from one repeat to the next in the 40mer spectra. Consistent with the ^{15}N-edited HSQC-monitored titration is the appearance of exchange-broadened ^{13}C peptide resonances for [peptide]/[Fab] molar ratios of >1 (Figure 3B,D).
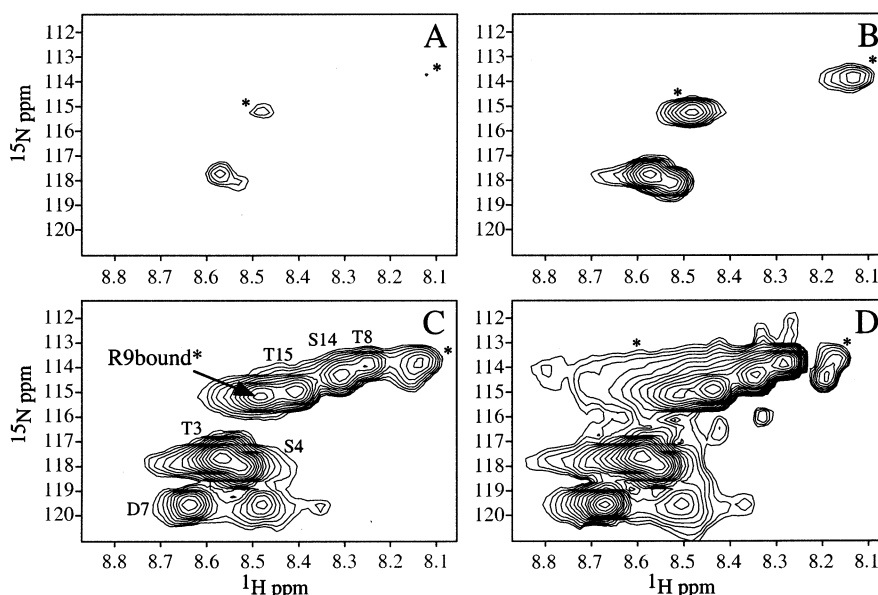
FIGURE 2: $^1H-^{15}N$ HSQC titration of 200 μM Fab B27.29 with MUC1 16mer peptide: (A) 40 μM 16mer, (B) 200 μM 16mer, (C) 500 μM 16mer, and (D) 800 μM 16mer. The Fab-bound peptide resonances are marked with asterisks, and increase in intensity until a peptide:Fab ratio of greater than 1:1 is reached. At a peptide:Fab ratio of greater than 1:1, the resonances of the MUC1 epitope sequence begin to appear, while the bound resonances do not increase in intensity. Notice that the resonances for Thr3 and Ser4 (near the end of the MUC1 peptide and outside the epitope sequence) have strong intensity throughout the titration. The spectra for the peptide with or without Fab were recorded at 500 MHz on a Varian Inova 500 NMR spectrometer. NMR samples were in PBS buffer (pH 7.1) and 90% H_2O/10% D_2O at 5.0 °C.

These resonances correspond to P6, D7, T8, R9, P10, A11, P12, and G13 within the 16mer (boxed in Figure 3B) and P5/25, D6/26, T7/27, R8/28, P9/29, A10/30, P11/31, and G12/32 within the 40mer (boxed in Figure 3D), an identical collection of residues that indicates identical binding epitopes in the one-repeat and two-repeat systems.

Taken together, the results of the ^{15}N-edited and ^{13}C-edited HSQC-monitored titrations are consistent and complementary. The exchange broadening observed for the PDTRPAP residues demonstrates selective interactions of this region of the sequence with Fab B27.29, in agreement with the epitope mapping of B27.29 provided by ELISA binding studies (*64*). Significantly, earlier NMR studies by this group have identified a type I β-turn spanning residues PDTR within the PDTRPAP epitope region of both the 16mer and the 40mer (*37, 38, 58*). These same studies also identified a second less well-defined β-turn in the 40mer, spanning residues GSTA immediately downstream of the peptide epitope region (*58*). However, the studies presented here demonstrate that only the glycine residue from the GSTA sequence (G13 in the 16mer and G12/32 in the 40mer) is exchange broadened in the presence of Fab. These results point to the specificity of the antibody as recognizing uniquely the PDTRPAP sequence, and not just general β-turn structure.

^{15}N NMR Relaxation Measurements. Once enough peptide was added to obtain sufficient intensity for the PDTRPAP resonances ([peptide]/[Fab] ≫ 1), NMR relaxation experiments were performed to probe the dynamics of the system. These experiments included the measurement of ^{15}N T_1 and T_2 relaxation rates and steady-state heteronuclear {^1H}−^{15}N NOEs for the ^{15}N- and ^{13}C-labeled 16mer and 40mer MUC1 peptides in the absence and presence of Fab B27.29. The values of these relaxation parameters are given in Tables S2−S4 of the Supporting Information. The ^{15}N T_1 relaxation

data from these tables are plotted in panels A (16mer with or without Fab) and B (40mer with or without Fab) of Figure 4.

In general, the ^{15}N T_1 and T_2 values acquired for the 16mer and 40mer MUC1 peptides become shorter in the presence of Fab, consistent with an overall increase in the correlation time of the peptides as they are bound to antibody. For example, the averaged ^{15}N T_1 value of the 16mer across the entire sequence ($\langle T_1 \rangle$) equals 767 ms in the absence of Fab, but $\langle T_1 \rangle = 508$ ms in the presence of Fab (800 μM 16mer and 200 μM Fab B27.29, or [peptide]/[Fab] = 4). The corresponding ^{15}N T_1 values for the 40mer ($\langle T_1 \rangle$) are 669 and 539 ms in the absence and presence, respectively, of the same relative ratios of Fab. These T_1 values show titration-dependent behavior (see panels A and B of Figure 4), in that an increase in the [peptide]/[Fab] ratio leads to a corresponding increase in the ^{15}N T_1 value measured for each residue in the peptide sequence. This concentration-dependent behavior demonstrates that the MUC1 peptide−Fab B27.29 complex experiences fast exchange behavior on the NMR relaxation time scale, and thus, the measured ^{15}N T_1 values are population-weighted averages of the free and bound states (see eq 6). Under these conditions, relaxation measurements made for exchange-broadened or even "free-state" peptide resonances (i.e., exchange being intermediate to slow on the chemical shift time scale) will nevertheless yield information relevant to the dynamics of the bound state. Thus, Fab-induced changes in the measured relaxation parameters can be interpreted within the context of Fab-induced changes to the backbone dynamics of the MUC1 peptides as these peptides are bound and immobilized within the B27.29-combining site.

^{13}C NMR Relaxation Measurements. While the ^{15}N NMR relaxation measurements discussed above provide evidence of fast exchange on the relaxation time scale, the Fab-induced
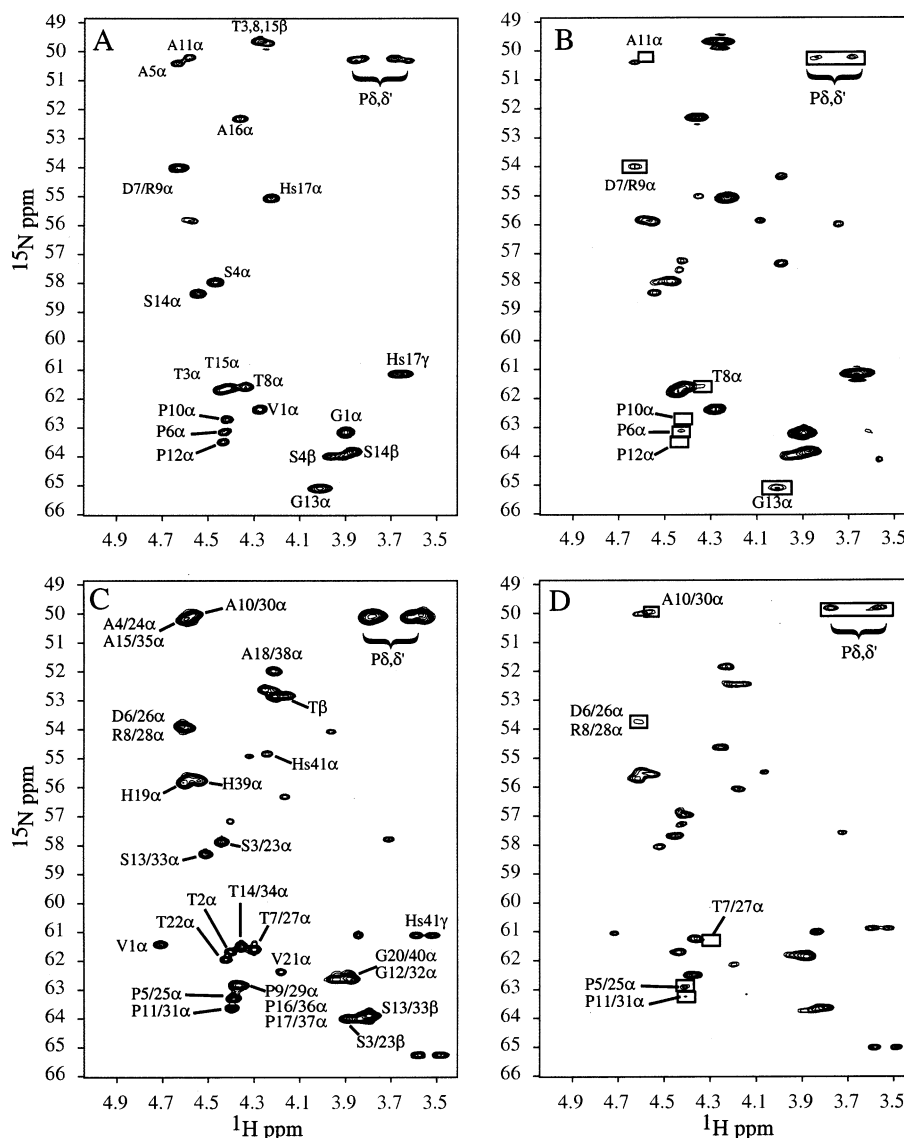
FIGURE 3: ^{1}H$-^{13}$C HSQC spectra of (A) 800 μM MUC1 16mer free in solution, (B) 500 μM 16mer with 200 μM Fab B27.29, (C) 800 μM 40mer free in solution, and (D) 200 μM 40mer with 200 μM Fab B27.29. Boxed cross-peaks experience the greatest losses in signal intensity due to line broadening in the presence of Fab. The spectra were recorded at 500 MHz on a Varian Inova 500 NMR spectrometer. NMR samples were in PBS buffer (pH 7.1) and 90% H_2O/10% D_2O at 5.0 °C.

changes measured for individual relaxation parameters (T_1, T_2, and NOE) are fairly uniform across the MUC1 peptide sequence. The limited sequence resolution afforded by the ^{15}N nucleus arises from the magnetic susceptibility of the ^{15}N$-^1$H bond vector to a variety of environmental influences, including changes in solvent exposure and solvent exchange. In contrast, the magnetic susceptibility of the ^{13}C$_\alpha-^1$H$_\alpha$ bond vector is uniquely sensitive to changes in local backbone conformation and chemical environment. Thus, ^{13}C NMR relaxation measurements can provide high-resolution, sequence-specific information about Fab-induced changes to the backbone dynamics of the MUC1 peptides, allowing a precise mapping of the boundaries of the peptide epitope recognized and bound by Fab B27.29. ^{13}C$_\alpha$ T_1 and $T_{1\rho}$ relaxation rates and steady-state heteronuclear {^{1}H$_\alpha$}$-^{13}$C$_\alpha$ NOEs were therefore also measured for the ^{15}N- and ^{13}C-labeled 16mer and 40mer MUC1 peptides in the absence and presence of Fab B27.29. The values of these relaxation parameters are presented in Tables S2$-$S4 of the Supporting Information.

Of the three parameters that were measured (T_1, $T_{1\rho}$, and NOE), the T_1 parameter arguably provides the best probe of local nanosecond to picosecond time scale dynamics, as it contains no exchange contributions,[3] nor does it suffer from low signal-to-noise or propagated error.[4]

Figure 5 therefore only presents the ^{13}C$_\alpha$ T_1 measured for the 16mer (panel A) and 40mer (panel B) MUC1 peptides in the absence (squares) and presence (circles) of Fab B27.29. In the presence of Fab, significant decreases in T_1 ($>$50 ms) are observed *only* for residues A5, P6, D7, R9, P10, A11, and P12 in the 16mer and P5/25, D6/26, T7/27, and R8/28

---

[3] The paramaters that measure transverse magnetization, $T_{1\rho}$ and T_2, contain a contribution from exchange between the free and bound state, according to the equation $R_{2obs} = P_B R_{2B} + P_F R_{2F} + P_B P_F(\tau)(2\pi\Delta\delta)^2$, where $\tau \sim 1/k_{-1}$ (compare to the analogous expression for R_{1obs} shown in eq 6).

[4] The steady-state heteronuclear NOE is calculated from difference spectra (with and without ^{1}H saturation), so experimental errors are summed. In addition, the spectrum acquired without ^{1}H saturation often suffers from a low to signal-to-noise ratio, contributing a significant error to the final calculated NOE.
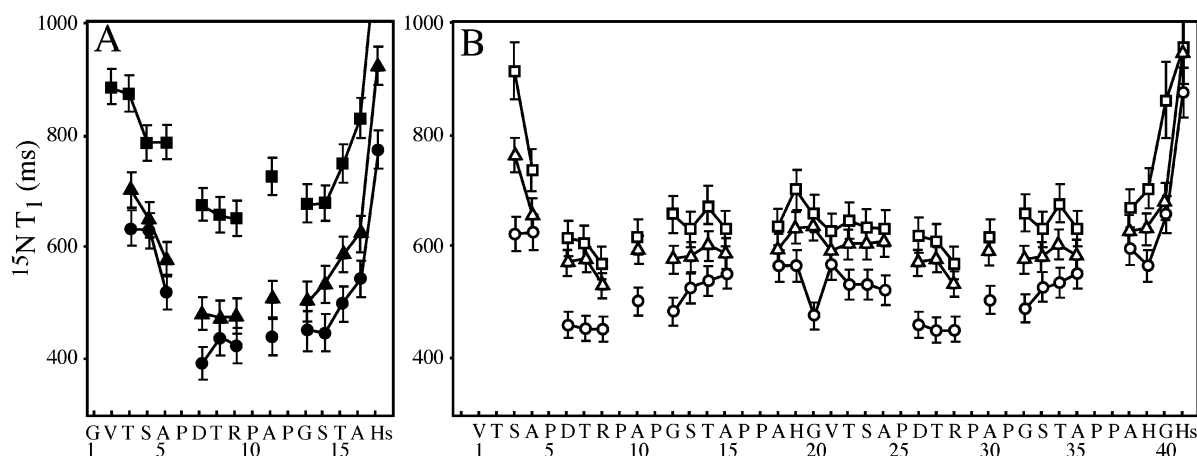
FIGURE 4: ^{15}N T_1 relaxation times measured for (A) 800 μM MUC1 16mer free in solution (■), 1600 μM 16mer with 200 μM Fab B27.29 (▲), and 800 μM 16mer with 200 μM Fab B27.29 (●) and (B) 800 μM 40mer free in solution (□), 1200 μM 40mer with 200 μM Fab B27.29 (△), and 800 μM 40mer with 200 μM Fab B27.29 (○). All measurements were taken at 500 MHz on a Varian Inova 500 NMR spectrometer. NMR samples were in PBS buffer (pH 7.1) and 90% H$_2$O/10% D$_2$O at 5.0 °C. Standard deviations calculated for each parameter are plotted as error bars.

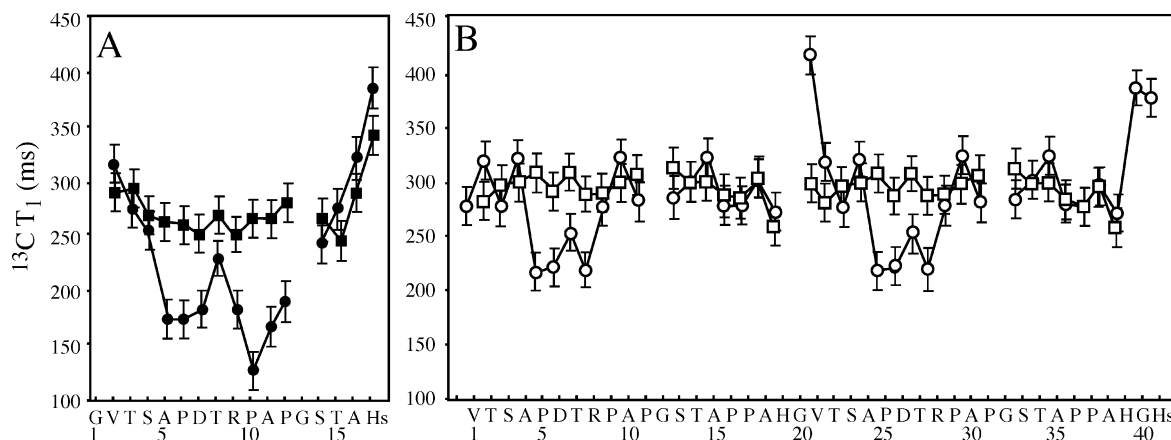FIGURE 5: ^{13}C$_\alpha$ T_1 relaxation times measured for (A) 800 μM MUC1 16mer free in solution (■) and 800 μM 16mer peptide with 200 μM Fab B27.29 (●) and (B) 40mer free in solution (□) and 800 μM 40mer peptide with 200 μM Fab B27.29 (○). All measurements were taken at 500 MHz on a Varian Inova 500 NMR spectrometer. NMR samples were in PBS buffer (pH 7.1) and 90% H$_2$O/10% D$_2$O at 5.0 °C. Standard deviations calculated for each parameter are plotted as error bars.

in the 40mer, indicating increases in the local correlation times of these PDTRPAP core epitope residues as they are bound and immobilized within the B27.29-combining site. That this collection of "bound and immobilized residues" differs somewhat between the two peptides (PDTR for the 40mer and APDTRPAP for the 16mer) is not a reflection of different binding modes. Rather, the disparity between the epitope profiles detected in the 16mer and the 40mer arises from the overlap of alanine and proline peaks in the 40mer T_1 spectra, which leads to averaged T_1 values measured for P9/29, P16/36, and P17/37, and for A4/24, A10/30, and A15/35 in the 40mer, and therefore artifically elevated values for P9/29 and A10/30 within the PDTRPAP core epitope. Thus, the epitope profile detected from the 16mer T_1 experiment probably best represents the true boundaries of the peptide epitope recognized and bound by Fab B27.29 (APDTRPAP), a profile which very closely matches that identified from earlier indirect ELISA-based experiments (PDTRPAP) (*10−15*).

Spectral Density Analysis. Raw relaxation rates are usually analyzed within the context of a relaxation formalism that can provide simplified motional models, as well as some insight into the time scales and amplitudes of internal

motions. One such formalism is the model free approach of Lipari and Szabo (*65, 66*), which provides a means of assessing the contributions of internal motions and conformational exchange to spin relaxation. However, there are limitations to this approach that arise from inherent assumptions. The overall molecular reorientation must be isotropic and independent of fast internal motions (which contribute negligibly to measured relaxation). These assumptions do not hold for small flexible peptides, like the MUC1 peptides, which can experience a broad range of motional time scales.

An alternative relaxation analysis approach for characterizing molecular dynamics is provided by spectral density analysis (*49, 50*) which has an advantage in that it makes no assumptions about the separability of the time scales between the motions, and allows the possibility of sizable contributions to relaxation from high-frequency motions. Moreover, this methodology is analytic and independent of error estimates. In general, the spectral density at $J(0)$ is proportional to the local correlation time of the backbone nitrogen (*67*). Thus, it is possible to interpret Fab binding-induced chances in $J(0)$ on the basis of changes in local correlation times. However, this interpretation is valid only in the absence of conformational exchange phenomena,
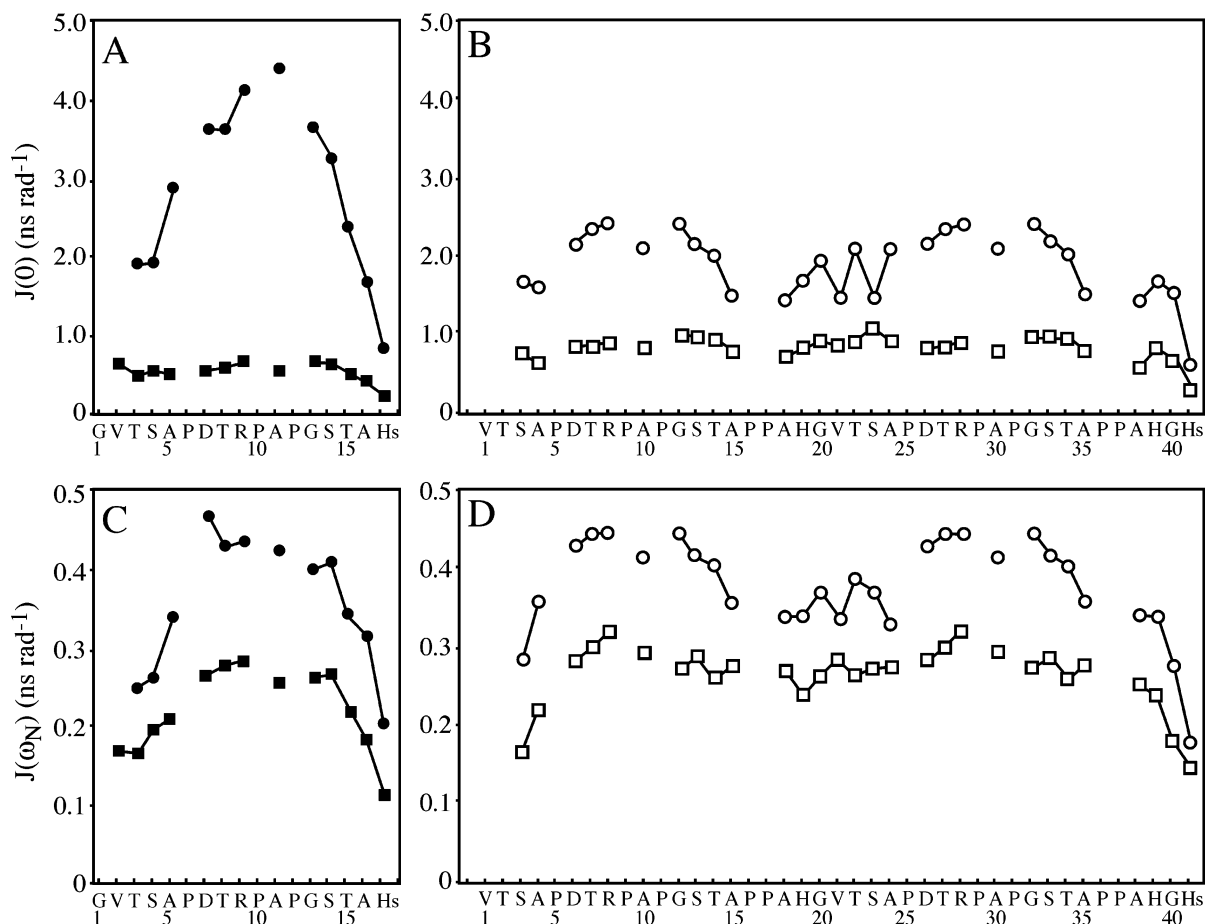
FIGURE 6: $J(0)$ and $J(\omega_N)$ spectral density values calculated from ^{15}N NMR relaxation data measured for (A and C) 800 μM MUC1 16mer free in solution (■) and 800 μM 16mer with 200 μM Fab B27.29 (●) and (B and D) 800 μM MUC1 40mer free in solution (□) and 800 μM 40mer with 200 μM Fab B27.29 (○). NMR samples were in PBS buffer (pH 7.1) and 90% H_2O/10% D_2O at 5.0 °C. Standard deviations calculated for each parameter are plotted as error bars.

which can lead to shortening of T_2 times, and therefore larger values of $J(0)$ (*68*). Therefore, the contribution of slow exchange motions (microseconds to milliseconds) to $J(0)$ must also be considered in spectral density analysis.

Using eqs 2−4 from Materials and Methods, the $J(\omega)$ spectral density values [$J(0)$, $J(\omega_N)$, and $J(\omega_H)$] were calculated from the ^{15}N T_1 and T_2 relaxation rates and the steady-state heteronuclear {^{1}H}−^{15}N NOEs measured for the ^{15}N- and ^{13}C-labeled MUC1 16mer and 40mer peptides free in solution versus those bound to Fab B27.29[5] (see Tables S2−S4 of the Supporting Information). These values are shown in Figure 6, which plots the $J(0)$ (panels A and B) and $J(\omega_N)$ (panels C and D) values only (see Table S5 of the Supporting Information for the raw values). The free peptide $J(0)$ (squares) yield average values across the entire sequence [$\langle J(0) \rangle$] of 0.53 ns rad^{-1} for the 16mer and 0.78 ns rad^{-1} for the 40mer, consistent with the longer global correlation time of the larger two-repeat peptide. In comparison, the average $J(0)$ value for the PDTRPAP epitope sequence [$\langle J(0) \rangle^{\text{epitope}}$] is 0.57 for the 16mer and 0.79 for the

40mer. Thus, the epitope sequences are not especially ordered relative to other parts of the sequence, at least in the free solution states of these peptides.

Addition of Fab (Figure 6, circles) leads to significant increases in the $J(0)$ values measured across the 16mer and 40mer sequences, commensurate with increases in the global correlation times experienced by these peptides as they are bound to antibody. These increases in $J(0)$ are not uniform across the length of the peptides, being the most pronounced for residues within the PDTRPAP epitope region. For example, $\langle J(0) \rangle$ for the entire 16mer sequence increases from 0.53 to 2.8 ns rad^{-1} (an increase of ~2.3 ns rad^{-1}), whereas $\langle J(0) \rangle^{\text{epitope}}$ for just the PDTRPAP epitope within the 16mer increases from 0.57 to 3.9 ns rad^{-1} (an increase of ~3.3 ns rad^{-1}). Similarly, $\langle J(0) \rangle$ for the entire 40mer sequence increases from 0.78 to 1.8 ns rad^{-1} (an increase of ~1.0 ns rad^{-1}), whereas $\langle J(0) \rangle^{\text{epitope}}$ increases from 0.79 to 2.2 ns rad^{-1} (an increase of ~1.4 ns rad^{-1}).[6] These substantially elevated $\langle J(0) \rangle^{\text{epitope}}$ values are consistent with significant increases in the local correlation times of residues that directly contact

---

[5] The reduced spectral density mapping approach assumes that the high-frequency spectral density terms are approximately equal in magnitude, i.e., $J(\omega_H \pm \omega_N) \approx J(\omega_H)$, and may therefore be replaced by a single equivalent term, $J(\omega_H)$ (*47*, *48*). This assumption does not hold for ^{13}C NMR relaxation, where $J(\omega_H \pm \omega_C)$ cannot be expected to equal $J(\omega_H)$. Thus, reduced spectral density terms were calculated only for the ^{15}N NMR relaxation data set.

[6] The stoichiometry of a 1:1 complex of 40mer and Fab results in an average of one bound 40mer epitope and one free 40mer epitope. Thus, the smaller increases in $J(0)$ measured for the 40mer versus the 16mer (at the same molar ratios of Fab to peptide) may be a result of the doubled effective ligand concentration of the 40mer, which presumably leads to a $J(0)$ value averaged between the one bound epitope and the one free epitope in the two-repeat peptide.
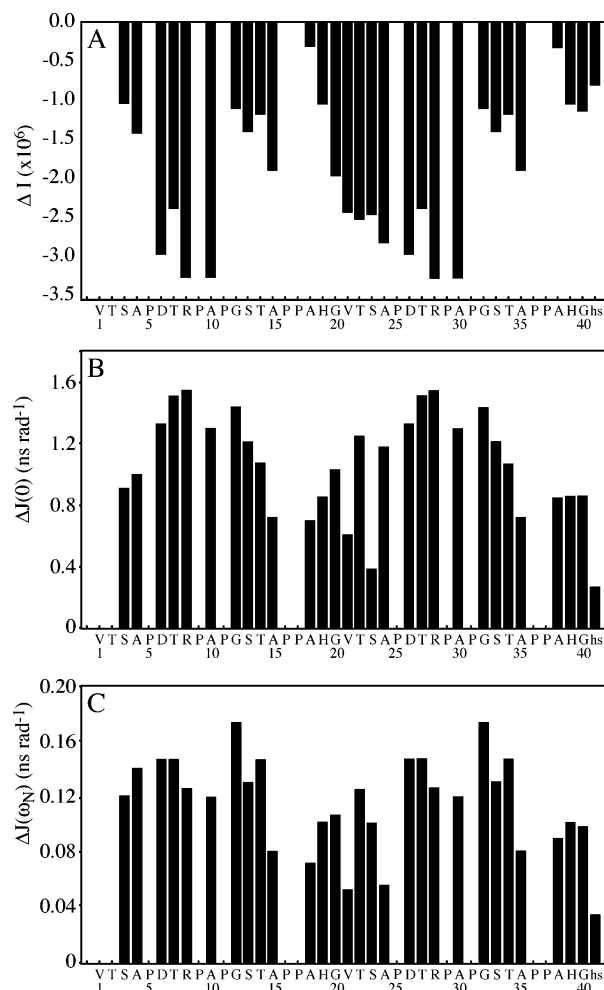
FIGURE 7: B27.29 epitope mapping of the MUC1 40mer peptide from analysis of line broadening and relaxation data. (A) Differences in the ^{1}H$-^{15}$N HSQC peak intensities (ΔI) measured for 400 μM 40mer with or without 200 μM Fab ($\Delta I = I^{+Fab} - I^{-Fab}$, where I^{+Fab} is the intensity of the peptide peak in the presence of Fab and I^{-Fab} is the intensity of the peptide peak in the absence of Fab). Negative values of ΔI indicate significant Fab-induced line broadening; i.e., $I^{+Fab} \ll I^{-Fab}$. (B) Differences in the $J(0)$ spectral density values [$\Delta J(0)$] calculated from ^{15}N NMR relaxation data measured for 400 μM 40mer with or without 200 μM Fab [$\Delta J(0) = J(0)^{+Fab} - J(0)^{-Fab}$, where $J(0)^{+Fab}$ is the $J(0)$ calculated for the peptide in the presence of Fab and $J(0)^{-Fab}$ is the $J(0)$ calculated for the peptide in the absence of Fab]. Increased values of $\Delta J(0)$ indicate significant Fab-induced increases in local correlation time; i.e., $J(0)^{+Fab} \gg J(0)^{-Fab}$. (C) Differences in the $J(\omega_N)$ spectral density values [$\Delta J(\omega_N)$] calculated from ^{15}N NMR relaxation data measured for 400 μM 40mer with or without 200 μM Fab [$\Delta J(\omega_N) = J(\omega_N)^{+Fab} - J(\omega_N)^{-Fab}$]. Fab-induced increases in $J(\omega_N)$ "track" Fab-induced increases in $J(0)$.

the antibody, well in excess of the uniform increases in global correlation time expected as a result of binding. Thus, the $J(0)$ spectral density terms calculated from ^{15}N NMR relaxation experiments are sensitive indicators of specific epitope−antibody interactions across the molecular interface, even if the constituent relaxation parameters (T_1, T_2, and NOE) appear to provide a less well-resolved picture upon first analysis.

As previously mentioned, conformational exchange processes on slow time scales can artificially elevate the value of $J(0)$ (68). However, these slow time scale motions have a negligible effect on the calculated values of the $J(\omega_N)$ and $J(\omega_H)$ spectral densities, as these represent only high-

frequency motions (49, 69, 70). Figure 6 (panels C and D) plots the $J(\omega_N)$ values calculated from the relaxation data presented in Table S5 of the Supporting Information. A comparison of the $J(\omega_N)$ and $J(0)$ plots reveals the same pattern of increases for PDTRPAP epitope residues, supporting our interpretation of increased local correlation times for these epitope residues upon antibody binding, and further confirming that exchange effects do not dominate the observed increases in $J(0)$. Most importantly, the quality of the $J(\omega_N)$ and $J(0)$ data presented for the MUC1 system illustrates the utility of spectral density analysis in epitope mapping, even in the presence of slow chemical exchange.

Peptide Epitope Mapping. In the study presented here, two different classes of isotope-edited NMR experiments have been used to map the binding of Fab B27.29 to one- and two-repeat MUC1 peptides: (1) HSQC-monitored titrations that measure exchange broadening, and therefore the relative magnitude of the Fab-induced chemical shift, and (2) NMR relaxation measurements that measure changes in the picosecond to nanosecond time scale motions in the peptide backbone as a function of Fab-induced increases in local correlation time. A comparison of the 40mer peptide epitope profiles obtained from ^{1}H$-^{15}$N HSQC-monitored spectral analysis versus ^{15}N NMR relaxation analysis is presented in Figure 7. The top panel (panel A) plots differences in the HSQC peak intensities (ΔI) as a consequence of Fab-induced chemical shifts, whereas the bottom two panels (panels B and C) plot differences in the low- and high-frequency spectral density values [$\Delta J(0)$ and $\Delta J(\omega_N)$] as a consequence of Fab-induced increases in local correlation time. As expected, these profiles show very similar trends, indicating that changes in the chemical environment track changes in local dynamics. Thus, regions of the 40mer peptide backbone that experience a marked change in chemical environment upon binding to B27.29 also show significant decreases in picosecond to nanosecond time scale motions as they become immobilized within the antibody-combining site. The consistency and complementarity of the information provided by these two independent NMR observables (chemical shift and spin relaxation) illustrate the power of a direct spectroscopic approach in peptide epitope mapping, especially if it can provide additional structural and dynamical information that is useful in peptide vaccine design.

CONCLUSIONS

We have developed an approach utilizing NMR relaxation measurements and heteronuclear correlation experiments to map antibody epitopes. These NMR experiments allow a direct, sequence-specific probe of binding, and clearly demonstrate which parts of the MUC1 peptide epitope are immobilized upon binding antibody. We apply this technique to determining the epitope of an antibody raised against tumor cells for the purposes of designing a cancer vaccine. Our method uses the antibody epitope as an indirect probe of a structural and/or dynamic state present on the tumor cell surface, and as a probe of the peptide state that is immunogenic. Our approach to vaccine design is of general utility for any antigen that lacks sufficient analytical characterization, as is the case with most tumor-associated antigens.

In this study, we provide direct spectroscopic evidence that the MUC1 peptide sequence PDTRPAP, portions of

Grinstead *et al.*

which were identified from earlier ELISA-based experiments as PDTRPA (*10−15*) and from our own previous homonuclear NMR studies of MUC1 glycopeptides as PDTRP (*37*), is bound and preferentially immobilized in the Fab B27.29-combining site. Immobilization of the entire PDTR-PAP sequence implies that the B27.29 epitope is continuous and all residues in the epitope contribute to the binding energy. Furthermore, we observe for the first time the bound-state resonance of arginine within the PDTRPAP epitope sequence. The observation of a bound-state resonance for arginine suggests that this residue makes intimate contact with B27.29, consistent with the mutational studies of Xing *et al.* (*12*). In addition, we show that the residues in the MUC1 sequence outside the boundaries of this defined epitope remain highly flexible in the bound state, demonstrating that they do not interact with antibody and extend into solution out of the antibody-combining site.

The heteronuclear NMR relaxation experiments in this study offer a significant increase in the amount of information available relative to that from previous homonuclear NMR experiments, in that individual proline resonances can now be assigned and monitored with ^{13}C labels (these were overlapped in the ^{1}H NMR spectrum), line broadening and doubling of resonances in NMR-monitored titrations interpreted within the context of exchange time scales and peptide backbone dynamics, and the limits of the peptide epitope bound and immobilized within the antibody-combining site more accurately mapped. Most importantly, analysis of ^{15}N and ^{13}C NMR relaxation data allows us to unequivocally demonstrate that the line broadening observed in our NMR-monitored titrations is a product of selective immobilization of the peptide epitope in the Fab binding site. Future studies will utilize the same heteronuclear NMR protocol to examine contributions of MUC1 tumor-associated carbohydrate to recognition by Fab B27.29. Those studies will allow a determination of how the carbohydrate interacts with antibody, as well as an elucidation of how carbohydrate affects the MUC1 peptide epitope.

Our characterization of the B27.29 epitope can be used to increase the immunogenicity of MUC1 peptide vaccine candidates. For example, since the MUC1 sequence outside the PDTRPAP epitope retains its conformational heterogeneity in the Fab-bound state and is not important for binding, it could be engineered for increased oral bioavailability, or to act as a linker for multiple PDTRPAP epitopes or other immunogenic peptide sequences. These changes could significantly improve the efficacy of a MUC1 peptide-based vaccine, while not altering the specificity of the immune response. In addition, our results suggest that since the PDTRPAP sequence is highly ordered in the antibody binding site, preordering of the structure of the vaccine candidate could increase the level of similarity with the immunologically relevant MUC1 structure and therefore increase immunogenicity. Future studies will continue to probe the structure of the antibody-bound MUC1 peptide sequence, with the ultimate goal of developing a second-generation MUC1 peptide vaccine that better represents the peptide portion of the tumor-associated MUC1 mucin.

SUPPORTING INFORMATION AVAILABLE

Resonance assignments, relaxation times, NOEs, and spectral density values. This material is available free of charge via the Internet at http://pubs.acs.org.

REFERENCES

1. Apostolopoulos, V., Sandrin, M. S., and McKenzie, I. F. C. (1999) *J. Mol. Med. 77*, 427−436.
2. Taylor-Papadimitriou, J., Burchell, J., Miles, D. W., and Dalziel, M. (1999) *Biochim. Biophys. Acta 1455*, 301−313.
3. Miles, D. W., and Taylor-Papadimitriou, J. (1999) *Pharmacol. Ther. 82*, 97−106.
4. Apostolopoulos, V., Pietersz, G. A., and McKenzie, I. F. (1999) *Curr. Opin. Mol. Ther. 1*, 98−103.
5. Van den Steen, P., Rudd, P. M., Dwek, R. A., and Opdenakker, G. (1998) *Crit. Rev. Biochem. Mol. Biol. 33*, 151−208.
6. Rudd, P. M., and Dwek, R. A. (1997) *Crit. Rev. Biochem. Mol. Biol. 32*, 1−100.
7. Carlstedt, I., and Davies, J. R. (1997) *Biochem. Soc. Trans. 25*, 214−219.
8. Koganty, R. R., Reddish, M. A., and Longenecker, B. M. (1997) in *Glycopeptides and Related Compounds: Synthesis, Analysis and Application*, pp 707−743, Dekker, New York.
9. Hanisch, F. G. (2001) *Biol. Chem. 382*, 143−149.
10. Girling, A., Bartkova, J., Burchell, J., Gendler, S., Gillett, C., and Taylor-Papadimitriou, J. (1989) *Int. J. Cancer 43*, 1072−1076.
11. Burchell, J., Taylor-Papadimitriou, J., Boshell, M., Gendler, S., and Duhig, T. (1989) *Int. J. Cancer 44*, 691−696.
12. Xing, P. X., Prenzoska, J., and McKenzie, I. F. (1992) *Mol. Immunol. 29*, 641−650.
13. Denton, G., Sekowski, M., and Price, M. R. (1993) *Cancer Lett. 70*, 143−150.
14. Kotera, Y., Fontenot, J. D., Pecher, G., Metzgar, R. S., and Finn, O. J. (1994) *Cancer Res. 54*, 2856−2860.
15. Bashford, J. L., Robins, R. A., and Price, M. R. (1993) *Int. J. Cancer 54*, 778−783.
16. Finn, O. J., Jerome, K. R., Henderson, R. A., Pecher, G., Domenech, N., Magarian-Blander, J., and Barratt-Boyes, S. M. (1995) *Immunol. Rev. 145*, 61−89.
17. Nakamura, H., Hinoda, Y., Nakagawa, N., Makiguchi, Y., Itoh, F., Endo, T., and Imai, K. (1998) *J. Gastroenterol. 33*, 354−361.
18. Petrarca, C., Casalino, B., von Mensdorff-Pouilly, S., Rughetti, A., Rahimi, H., Scambia, G., Hilgers, J., Frati, L., and Nuti, M. (1999) *Cancer Immunol. Immunother. 47*, 272−277.
19. Ding, L., Lalani, E. N., Reddish, M., Koganty, R., Wong, T., Samuel, J., Yacyshyn, M. B., Meikle, A., Fung, P. Y., and Taylor-Papadimitriou, J. (1993) *Cancer Immunol. Immunother. 36*, 9−17.
20. Jerome, K. R., Barnd, D. L., Bendt, K. M., Boyer, C. M., Taylor-Papadimitriou, J., McKenzie, I. F., Bast, R. C., Jr., and Finn, O. J. (1991) *Cancer Res. 51*, 2908−2916.
21. Musselli, C., Ragupathi, G., Gilewski, T., Panageas, K. S., Spinat, Y., and Livingston, P. O. (2002) *Int. J. Cancer 97*, 660−667.
22. Mitchell, M. S. (2002) *Curr. Opin. Invest. Drugs 3*, 150−158.
23. Pecher, G., Haring, A., Kaiser, L., and Thiel, E. (2002) *Cancer Immunol. Immunother. 51*, 669−673.
24. Brossart, P., Wirths, S., Stuhler, G., Reichardt, V. L., Kanz, L., and Brugger, W. (2000) *Blood 96*, 3102−3108.
25. Foon, K. A. (2001) *Curr. Oncol. Rep. 3*, 116−126.
26. Morse, M. A. (2000) *Curr. Opin. Mol. Ther. 2*, 453−458.
27. Morse, M. A. (2001) *Curr. Opin. Mol. Ther. 3*, 102−105.
28. Doehn, C., and Jocham, D. (2000) *Curr. Opin. Mol. Ther. 2*, 106−111.
29. Denda-Nagai, K., and Irimura, T. (2000) *Glycoconjugate J. 17*, 649−658.
30. Nishimori, I., Perini, F., Mountjoy, K. P., Sanderson, S. D., Johnson, N., Cerny, R. L., Gross, M. L., Fontenot, J. D., and Hollingsworth, M. A. (1994) *Cancer Res. 54*, 3738−3744.
31. Nishimori, I., Johnson, N. R., Sanderson, S. D., Perini, F., Mountjoy, K., Cerny, R. L., Gross, M. L., and Hollingsworth, M. A. (1994) *J. Biol. Chem. 269*, 16123−16130.

32. Wandall, H. H., Hassan, H., Mirgorodskaya, E., Kristensen, A. K., Roepstorff, P., Bennett, E. P., Nielsen, P. A., Hollingsworth, M. A., Burchell, J., Taylor-Papadimitriou, J., and Clausen, H. (1997) *J. Biol. Chem. 272*, 23503−23514.

33. Muller, S., Goletz, S., Packer, N., Gooley, A., Lawson, A. M., and Hanisch, F. G. (1997) *J. Biol. Chem. 272*, 24780−24793.

34. Muller, S., Alving, K., Peter-Katalinic, J., Zachara, N., Gooley, A. A., and Hanisch, F. G. (1999) *J. Biol. Chem. 274*, 18165−18172.

35. Fontenot, J. D. (1993) *Cancer Res. 53*, 5386−5394.

36. Liu, X., Sejbal, J., Kotovych, G., Koganty, R. R., Reddish, M. A., Jackson, L., Gandhi, S. S., Mendonca, A. J., and Longenecker, B. M. (1995) *Glycoconjugate J. 12*, 607−617.

37. Grinstead, J. S., Koganty, R. R., Krantz, M. J., Longenecker, B. M., and Campbell, A. P. (2002) *Biochemistry 41*, 9946−9961.

38. Schuman, J., Campbell, A. P., Koganty, R. R., and Longenecker, B. M. (2003) *J. Pept. Res. 61*, 91−108.

39. Fontenot, J. D., Finn, O. J., Dales, N., Andrews, P. C., and Montelaro, R. C. (1993) *Pept. Res. 6*, 330−336.

40. Fontenot, J. D., Mariappan, S. V., Catasti, P., Domenech, N., Finn, O. J., and Gupta, G. (1995) *J. Biomol. Struct. Dyn. 13*, 245−260.

41. Kuliopulos, A., and Walsh, C. T. (1994) *J. Am. Chem. Soc. 116*, 4599−4607.

42. Farrow, N. A., Muhandiram, R., Singer, A. U., Pascal, S. M., Kay, C. M., Gish, G., Shoelson, S. E., Pawson, T., Forman-Kay, J. D., and Kay, L. E. (1994) *Biochemistry 33*, 5984−6003.

43. Yamazaki, T., Muhandiram, R., and Kay, L. E. (1994) *J. Am. Chem. Soc. 116*, 8266−8278.

44. Wittekind, M., and Mueller, L. (1993) *J. Magn. Reson., Ser. B 101*, 201.

45. Grzesiek, S., and Bax, A. (1992) *J. Am. Chem. Soc. 114*, 6291−6293.

46. Delaglio, F., Grsesiek, S., Vuister, G. W., Zhu, G., Pfeifer, J., and Bax, A. (1995) *J. Biomol. NMR 6*, 277−293.

47. Volkman, B. F., Alam, S. L., Satterlee, J. D., and Markley, J. L. (1998) *Biochemistry 37*, 10906−10919.

48. Zhang, P., Dayie, K. T., and Wagner, G. (1997) *J. Mol. Biol. 272*, 443−455.

49. Peng, J. W., and Wagner, G. (1995) *Biochemistry 34*, 16733−16752.

50. Farrow, N. A., Zhang, O., Forman-Kay, J. D., and Kay, L. E. (1995) *Biochemistry 34*, 868−878.

51. Foote, J., and Eisen, H. N. (1995) *Proc. Natl. Acad. Sci. U.S.A. 92*, 1254−1256.

52. Northrup, S. H., and Erickson, H. P. (1992) *Proc. Natl. Acad. Sci. U.S.A. 89*, 3338−3342.

53. Raman, C. S., Jemmerson, R., Nall, B. T., and Allen, M. J. (1992) *Biochemistry 31*, 10370−10379.

54. Karlsson, R., and Falt, A. (1997) *J. Immunol. Methods 200*, 121−133.

55. Gemmecker, G. (1999) in *NMR as a Tool in Drug Research* (Holzgrabe, U., Wawer, I., and Diehl, B., Eds.) pp 140−141, Wiley, New York.

56. Lian, L. Y., Barsukov, I. L., Sutcliffe, M. J., Sze, K. H., and Roberts, G. C. (1994) *Methods Enzymol. 239*, 657−700.

57. Campbell, A. P., and Sykes, B. D. (1993) *Annu. Rev. Biophys. Biomol. Struct. 22*, 99−122.

58. Schuman, J., Grinstead, J. S., and Campbell, A. P. (2003) *Biochemistry*, submitted.

59. Koebnik, R., Locher, K. P., and Van Gelder, P. (2000) *Mol. Microbiol. 37*, 239−253.

60. Zvi, A., Tugarinov, V., Faiman, G. A., Horovitz, A., and Anglister, J. (2000) *Eur. J. Biochem. 267*, 767−779.

61. Tugarinov, V., Zvi, A., Levy, R., and Anglister, J. (1999) *Nat. Struct. Biol. 6*, 331−335.

62. Stanfield, R., Cabezas, E., Satterthwait, A., Stura, E., Profy, A., and Wilson, I. (1999) *Struct. Folding Des. 7*, 131−142.

63. Derrick, J. P., Maiden, M. C., and Feavers, I. M. (1999) *J. Mol. Biol. 293*, 81−91.

64. Price, M. R., Rye, P. D., Petrakou, E., Murray, A., Brady, K., Imai, S., Haga, S., Kiyozuka, Y., Schol, D., Meulenbroek, M. F., Snijdewint, F. G., von Mensdorff-Pouilly, S., Verstraeten, R. A., Kenemans, P., Blockzjil, A., Nilsson, K., Nilsson, O., Reddish, M., Suresh, M. R., Koganty, R. R., Fortier, S., Baronic, L., Berg, A., Longenecker, M. B., Hilgers, J., *et al.* (1998) *Tumor Biol. 19* (Suppl. 1), 1−20.

65. Lipari, G., and Szabo, A. (1982) *J. Am. Chem. Soc. 104*, 4546−4559.

66. Lipari, G., and Szabo, A. (1982) *J. Am. Chem. Soc. 104*, 4559−4570.

67. Peng, J. W., and Wagner, G. (1992) *Biochemistry 31*, 8571−8586.

68. Davis, J. H., and Agard, D. A. (1998) *Biochemistry 37*, 7696−7707.

69. Bhattacharya, S., Botuyan, M. V., Hsu, F., Shan, X., Arunkumar, A. I., Arrowsmith, C. H., Edwards, A. M., and Chazin, W. J. (2002) *Protein Sci. 11*, 2316−2325.

70. Lefevre, J. F., Dayie, K. T., Peng, J. W., and Wagner, G. (1996) *Biochemistry 35*, 2674−2686.